

Observations of Centrally Peaked Impurity Profiles Following Pellet Injection in the Alcator-C Tokamak

R. D. Petrasso, D. J. Sigmar, K. W. Wenzel, J. E. Hopf, M. Greenwald, J. L. Terry, and J. Parker

Massachusetts Institute of Technology, Cambridge, Massachusetts 02139

(Received 11 December 1985)

Highly peaked carbon and molybdenum profiles occurred after hydrogen pellet injection. 40 ms after injection, carbon was well fitted by $[T_e/T_e(0)]^{1.5Z_C}$ for $r \leq 6.5$ cm ($Z_C=6$). Experimental values of the inward convective velocity and diffusivity were $\sim 10^3(r/a)$ cm/s and ~ 300 cm²/s, respectively, which are of the order of neoclassical predictions. An internal disruption then occurred, which reduced on-axis impurities by $\frac{2}{3}$ and ended neoclassical-like transport. Carbon is also found to affect sawtooth dynamics dramatically by altering the central resistivity. The implications of these observations for ignited plasmas are discussed.

PACS numbers: 52.25.Fi, 52.25.Vy, 52.70.La

Substantial progress towards fusion conditions has been made in the confinement, stability, and heating of magnetically confined plasmas in toroidal (tokamak) geometries. However, despite a decade of intensive work on the critical problem of impurity transport in tokamaks, it has remained an elusive and complicated issue.¹⁻³ Besides energy losses from impurity-line radiation, one has to be concerned about dilution of fuel-ion density due to impurities, and about effects impurities may have on main ion and electron transport. Usually impurity transport has been characterized as very different from the predictions of neoclassical theory.²⁻⁴ In the infrequent instances when transport was explicitly suggested to be neoclassical-like,¹ this inference was not based upon spatial profiles of the impurities and their time evolution. However, without such detailed information, as well as knowledge of the *absolute* abundances of the principal impurities, it is not possible to quantify the exact character of the impurity transport, be it neoclassical or some other theory of transport. More recent work has started to focus on this issue.⁵

Here we report the simultaneous measurements of the absolute abundances of the Alcator-C tokamak's main light (carbon) and heavy (molybdenum) impurities. Through the use of two absolutely calibrated x-ray arrays, time-resolved impurity profiles were obtained for plasma discharges in which frozen hydrogen pellets were used for plasma fueling. An intriguing feature of these experiments is that the pellet is found to affect impurity transport and profiles dramatically. In particular carbon, the dominant nonhydrogenic contributor to the plasma resistivity, is characterized by a flat profile prior to pellet injection, but a centrally peaked one some 40 ms afterwards. In fact, within experimental uncertainty, the peaked profile is well described by neoclassical predictions. Additionally, the post-pellet peaking of carbon is also found to be directly linked to a dramatic lengthening (or total inhibition) of sawtooth oscillations. This effect results

from the central "flattening" of the current-density profile, a consequence of the plasma resistivity's peaking in tandem with the carbon. In this paper we summarize a large body of data on these pellet-induced impurity transport changes by focusing on a representative discharge. (Many additional details are given by Petrasso *et al.*⁶)

The starting point for our analysis involves determination of the carbon (n_C) and molybdenum (n_{Mo}) densities from the two equations

$$\epsilon^A/n_e - P_H^A n_H \approx P_C^A n_C + P_{Mo}^A n_{Mo}, \quad (1)$$

$$\epsilon^B/n_e - P_H^B n_H \approx P_C^B n_C. \quad (2)$$

ϵ^A and ϵ^B are the absolute x-ray emissivities determined from Abel inversion of x-ray array data (arrays *A* and *B*); n_e is the electron density, determined from interferometer and Thomson-scattering measurements; $n_H = n_e - Z_C n_C - Z_{Mo} n_{Mo}$ ($Z_C=6$, $Z_{Mo} \approx 30$, and $Z_{Mo} n_{Mo}$ is negligible); and the P_j^k 's are spectral power functions for each radiating ion species j , where j stands for H, C, or Mo, and k represents either array *A* or *B*. Figure 1(a) shows the spectral efficiencies of the two arrays, and Fig. 1(b) depicts array-*B* power functions for fully stripped hydrogen and carbon ions.^{6,7} For array *B* and relevant Alcator conditions, only $\sim 2\%$ of detected x rays are from molybdenum ions. This is primarily because the filter greatly reduces the intense $\Delta n=1$ transitions that occur around 2.5 keV [see Fig. 1(a)].

Time traces of several adjacent x-ray detectors are shown in Fig. 2 for a representative discharge in which the plasma current is 520 kA and the toroidal field is 9.7 T (major and minor radii of 64 and 16.5 cm). As the pellet enters the plasma, the signals drop as $T_e(0)$ plummets from 1.6 to 0.6 keV. During the next 37 ms, T_e recovers and the carbon profile inside 7 cm gradually evolves from a flat prepellet profile to a highly peaked one. The profile then abruptly flattens at the giant impurity disruption (henceforth abbreviat-

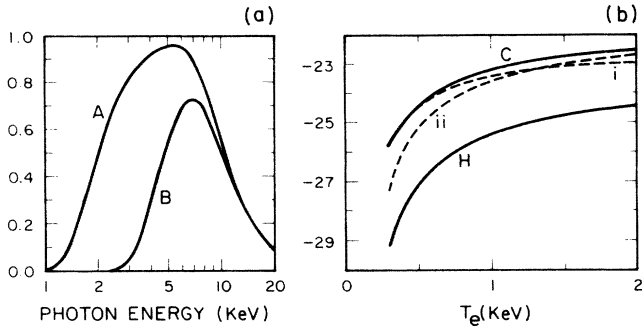


FIG. 1. (a) X-ray spectral efficiencies for arrays *A* and *B*. The low-energy response results mainly from 10.0 mg/cm² Be for *A*, and from 10.0 mg/cm² Be plus 30.4 mg/cm² C for *B*. The high-energy response results from the finite detector thickness (23.3 mg/cm² Si). (b) Array-*B* power functions for hydrogen (H) and carbon (C) x-ray continua. Recombination (curve i) and bremsstrahlung (curve ii) components of carbon are individually depicted, the former dominating for $T_e < 1.3$ keV (units of erg cm³/s; vertical scale in log₁₀).

ed as GID), and thereafter carbon does not dramatically repeat. From pellet injection until the GID, the carbon profile is modulated by sawteeth of increasing duration. Indeed, there are many discharges in which, following pellet injection, sawtoothing eventually stops altogether (without major disruptions ensuing). Figure 2(c) depicts x-ray emissivity profiles at critical times in the discharge of Figs. 2(a) and 2(b). Contrary to "giant" internal disruptions attributed to large temperature fluctuations,⁸ the GID is of a different nature [notice the small temperature drop in Fig. 3(d)]. In fact the temperature perturbation of the significantly smaller internal disruption following the GID [Fig. 2(a)] is virtually identical to that of the GID.

Figures 3(a) and 3(b) show the experimentally determined carbon and molybdenum density profiles just prior to and after the GID. The dashed curves are the asymptotic equilibrium profiles predicted on the basis of multi-ion neoclassical theory.⁹ In comparing experiment with theory, note that carbon is in the plateau regime (i.e., the carbon collision frequency is less than the transit frequency). Also because of small molybdenum concentrations, diffusion of carbon is governed by its interaction with hydrogenic (H) ions. Thus the expression for the radial carbon flux is^{2,9}

$$\Gamma_C \propto \left[\frac{n'_H}{n_H} - \frac{n'_C}{Z_C n_C} + \frac{1.5T'}{T} \right], \quad (3)$$

where T'/T is assumed the same for electrons and ions, and the prime indicates differentiation with respect to r . The source-free equilibrium solution to the continuity equation

$$\partial n_C / \partial t + \nabla \cdot \Gamma_C = 0 \quad (4)$$

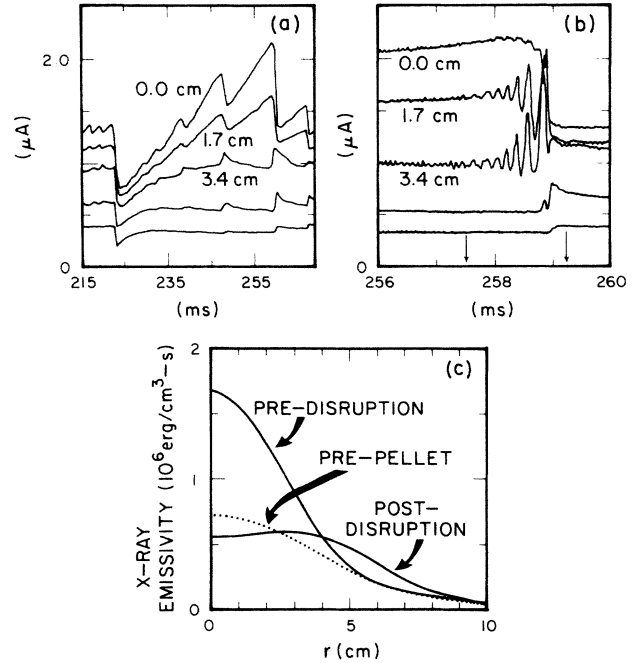


FIG. 2. (a) Several x-ray signals for adjacent array-*A* detectors viewing chords separated by 1.7 cm (shot No. 25). The 0-cm signal corresponds to the center-viewing detector. The pellet enters the plasma at about 223 ms; the giant impurity disruption (GID) occurs at about 259 ms (units of microamperes). (b) Same as (a), but time-expanded about the GID; the arrows indicate times of analysis for all subsequent figures. (c) Absolute array-*A* x-ray emissivities (determined from Abel inversion) just before the pellet (dotted line), and just before (257.5 ms) and after (259.3 ms) the GID (solid lines).

is, with use of Eq. (3),

$$\left(\frac{n_C}{n_C(0)} \right) = \left(\frac{n_H}{n_H(0)} \right)^{Z_C} \left(\frac{T}{T(0)} \right)^{1.5Z_C}. \quad (5)$$

Equation (5) predicts that the temperature profile is responsible for the peaking of carbon since n_H is slightly hollow because of central ion-deficit effects [Fig. 3(e)]. Because the experimental (predisruption) temperature profile is well represented by a Gaussian, Eq. (3) can be accurately recast as

$$\Gamma_C = -Dn'_C - n_C V(r/a) \quad (r \leq 6 \text{ cm}), \quad (6)$$

where a is the minor radius (16.5 cm). The solution of Eq. (6) for $\Gamma_C = 0$ is $n_C \propto \exp[-r^2/(2aD/V)]$. From the experimental data at 257.5 ms [see Fig. 2(b)] D/V is $0.33 \pm_{0.13}^{0.18}$ cm.

From the carbon peaking that occurs in the 12-ms interval preceding the GID [see Fig. 2(a)], V and D have been determined inside 4 cm; they are of order 10³ cm/s and 300 cm²/s, respectively. The corresponding theoretical values are 500 cm/s and 150 cm²/s. Thus the measured values are of the order of

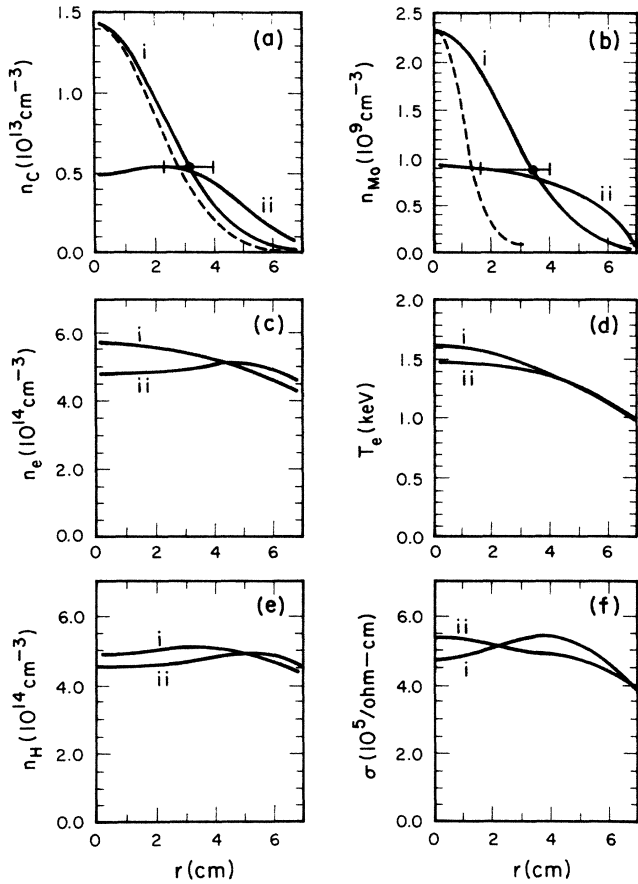


FIG. 3. Measured profiles before (curves i) and after (curves ii) the giant impurity disruption (GID) at the times indicated in Fig. 2(b). (a) Carbon density profiles. (b) Same as for (a), but for molybdenum. Outside of ~ 6.5 cm, the ratio of impurity to electron density increases. The dashed curves are the predictions of Eqs. (5) and (7). (c) Corresponding n_e profiles. (d) Corresponding T_e profiles. (e) Corresponding n_H profiles. (f) Corresponding Spitzer conductivity profiles. The relative error in the conductivity profile is $\leq 5\%$, the absolute error $< 15\%$.

the neoclassical predictions. In contrast most tokamaks,^{2,3} including Alcator for nonpellet (or prepellet) discharges,⁴ have typically reported empirical diffusivities that are 1 to 2 orders of magnitude larger than neoclassical predictions.

The dashed curve in Fig. 3(b) depicts the asymptotic source-free equilibrium profile for molybdenum, predicted by the appropriate mixed-regime theory^{6,9} (molybdenum in the Pfirsch-Schlüter regime, carbon and hydrogen in the plateau regime). Peaking of molybdenum is significantly driven by the carbon profile,⁶ yielding a Taylor-type solution¹⁰

$$\left(\frac{n_{\text{Mo}}}{n_{\text{Mo}}(0)} \right) \approx \left(\frac{n_{\text{C}}}{n_{\text{C}}(0)} \right)^{(Z_{\text{Mo}}/Z_{\text{C}})\bar{\lambda}} \quad (r \leq 4 \text{ cm}), \quad (7)$$

where $\bar{\lambda} \approx 0.73$ and is due to collision frequencies and

mass ratios.⁶ Temperature and hydrogen gradients are subdominant in shaping molybdenum profiles for $r \leq 4$ cm. Because of larger uncertainty in the experimental molybdenum profile, the experimental width is between a factor of 1.3 and 3.0 that of Eq. (7). From the theoretical viewpoint, however, it is important to include impurity-electron friction [as represented through Eq. (9) for ambipolar balance]. Specifically, molybdenum is a trace impurity, i.e., $\alpha_{\text{Mo}} = n_{\text{Mo}}Z_{\text{Mo}}^2/n_{\text{H}} \sim 3 \times 10^{-3} \ll (m_e/m_{\text{H}})^{1/2}$, while carbon is a major impurity, $\alpha_{\text{C}} = n_{\text{C}}Z_{\text{C}}^2/n_{\text{H}} \sim 1 \gg (m_e/m_{\text{H}})^{1/2}$. Thus for carbon the standard neoclassical treatment, which drops the carbon-electron friction versus the carbon-hydrogen friction, is justified, i.e., to zeroth order in $(m_e/m_{\text{H}})^{1/2}$

$$(\Gamma_{\text{H}} + Z_{\text{C}}\Gamma_{\text{C}})^{(0)} \approx 0. \quad (8)$$

(Carbon-molybdenum friction is also negligible.) For the molybdenum test particles, however, the full ambipolar balance must be considered, i.e., through first order

$$Z_{\text{Mo}}\Gamma_{\text{Mo}} = \Gamma_e - (\Gamma_{\text{H}} + Z_{\text{C}}\Gamma_{\text{C}})^{(1)}. \quad (9)$$

Experimental estimates of the right-hand side of Eq. (9) yield a small net positive (i.e., radially outward) contribution ($\Gamma_e \leq 10^{14} \text{ cm}^{-2} \text{ s}^{-1}$ at ~ 4 cm), which has the effect of broadening the molybdenum equilibrium profile of Eq. (7) by a factor of 2. Thus inclusion of electron friction brings the theoretical prediction well within experimental uncertainty.

Finally we posit that central carbon, the dominant nonhydrogenic contributor to Z_{eff} , has directly measurable effects on the dynamics of the sawtooth period.¹¹ As carbon gradually peaks following the pellet, the central Spitzer conductivity (calculated on the basis of the measured carbon, molybdenum, and T_e profiles of Fig. 3; molybdenum contributes insignificantly) will hollow, leading to a flattening—possibly a hollowing—of the current profile [see curve i of Fig. 3(f)].¹² If the current is sufficiently flat, the safety factor should be above 1 everywhere in the plasma. Indeed, this may account for numerous discharges where sawteeth are completely suppressed following pellet injection. (Major disruptions do not ensue for these cases.) In this situation highly peaked impurity profiles persist even while the temperature remains peaked on axis. It is important to stress that this sawtooth suppression is not a result of a major change in central radiative power balance since, for the discharges discussed here, radiation plays an insignificant role in the central power balance. (See Ref. 1 and Isler *et al.*¹³ for experiments in which central radiation is significant, sawtoothing stops, and the plasma disrupts.) Equally relevant to the connection between the peakedness of the carbon profile and the sawtooth period is the observation that the carbon profile does

not dramatically reappear after the GID. Just after the GID the measured conductivity peaks [curve ii of Fig. 3(f)] and, subsequently, the sawtooth period progressively shortens (by a factor of 2.5 approximately 15 ms after the GID of Fig. 2).

In summary, differently filtered x-ray arrays have been used to measure simultaneously centrally peaked carbon and molybdenum profiles following pellet injection. Central values of the diffusivity and convective velocity for carbon, as well as the width of the carbon profile inside 6.5 cm, are close to neoclassical predictions. The peaked molybdenum profile, which has a larger experimental uncertainty, is between a factor of 1.3 and 3.0 times that of the asymptotic neoclassical prediction [Eq. (7)]; theory suggests, however, that the asymptotic profile should not be realized as long as there is a significant radial outward flux of electrons (which is experimentally observed). We have no proven explanation why the pellet affects the impurity transport in the manner described, whereas for non-pellet discharges Alcator impurity transport,⁴ as well as impurity transport on most other tokamaks,² has been observed to be strongly variant from neoclassical predictions. However, the hypothesis has been raised that pellet injection¹⁴ lowers $\eta_i = \partial \ln T / \partial \ln n$ by a factor 2, thereby stabilizing the "ion mixing mode"¹⁵ and permitting classical ion transport to evolve. Regarding the evolution of sawteeth, we have presented experimental evidence that the central peaking (flattening) of carbon is directly linked to the lengthening (shortening) of the sawtooth period—or stops the sawtooth altogether—through corresponding changes in the central Spitzer conductivity profile.

From these observations there arises the concern that the thermalized alpha component of an ignited deuterium-tritium plasma may be strongly peaked on axis, depending on ion particle transport and sawtooth activity in pellet-fueled plasmas. And conversely, with increasing central impurity peaking, the current density may flatten, thereby greatly extending the sawtooth period or even suppressing sawteeth entirely. Since this may produce intolerably good impurity confinement, our observations imply that recent suggestions of rf stabilization of the $m = 1$ island, in order to permit sawtooth-free operation for $q(0) < 1$, may have to be modified to allow periodic impurity expulsion via a

deliberately induced internal giant impurity disruption.

We thank S. Wolfe, C. Gomez, M. Foord, E. Marmor, R. Granetz, and J. Rice for interferometer, electron cyclotron, visible bremsstrahlung, and x-ray data. For assistance early in this program, we thank N. Loter and F. Seguin. This work has been supported in part by Department of Energy Contract No. DE-AC02-78ET51013.

¹W. Engelhardt *et al.*, International Atomic Energy Agency Report No. IAEA-CN-37/A-5, 1978 (unpublished), p. 123.

²TFR Group, Nucl. Fusion **22**, 1173 (1982), and references therein.

³R. C. Isler, Nucl. Fusion **24**, 1599 (1984), and references therein.

⁴E. Marmor, J. Rice, J. Terry, and F. Seguin, Nucl. Fusion **22**, 1567 (1982), and references therein.

⁵K. Ida, R. Fonck, S. Sesnic, R. Hulse, and B. LeBlanc, Princeton Plasma Physics Laboratory Reports No. PPPL 2264, 1985 (unpublished), and No. PPPL 2313, 1986 (unpublished).

⁶R. D. Petrasso *et al.*, Massachusetts Institute of Technology Plasma Fusion Center Reports No. PFC/JA-85-41, 1985 (unpublished), and No. PFC/JA-86-26, 1986 (unpublished); J. Hopf, senior thesis, Massachusetts Institute of Technology, Physics Department, 1986 (unpublished).

⁷R. D. Petrasso *et al.*, Rev. Sci. Instrum. **51**, 585 (1980), and Phys. Rev. Lett. **49**, 1826 (1982).

⁸W. Pfeiffer *et al.*, Nucl. Fusion **25**, 655 (1985).

⁹S. P. Hirshman and D. J. Sigmar, Nucl. Fusion **21**, 1079 (1981); Eq. (6.129) for Mo; Eqs. (7.43)–(7.48) for C in the plateau regime; Eq. (6.75) for C if in the Pfirsch-Schlüter regime; references therein. More details are given in Ref. 6.

¹⁰J. B. Taylor, Nucl. Fusion, Suppl. 403 (1974).

¹¹G. L. Jahns *et al.*, Nucl. Fusion **22**, 1049 (1982); R. E. Denton, J. F. Drake, R. G. Kelva, and D. A. Boyd, Phys. Rev. Lett. **56**, 2477 (1986).

¹²This can be seen from the current-density diffusion equation (Ref. 6) when the large radial variation of the gradient of the Spitzer resistivity η due to impurity peaking is included.

¹³R. C. Isler, W. L. Rowan, and W. L. Hodge, Phys. Rev. Lett. **55**, 2413 (1985).

¹⁴S. Wolfe *et al.*, Nucl. Fusion **26**, 329 (1986).

¹⁵T. Antonsen, B. Coppi, and R. Englade, Nucl. Fusion **19**, 641 (1979).